Capillary rise in sharp corners: not quite universal

Katie Wu[1]†, C. Duprat[2], and H. A. Stone[1]‡

[1]Department of Mechanical and Aerospace Engineering, Princeton University, Princeton, NJ 08544, USA

[2]Laboratoire d'Hydrodynamique (LadHyX), École Polytechnique, Rte de Saclay, 91120 Palaiseau, France

(Received xx; revised xx; accepted xx)

We study the capillary rise of viscous liquids into sharp corners formed by two surfaces whose geometry is described by power laws, $h_i(x) = c_i x^n$, $i = 1, 2$, where $c_2 > c_1$ for $n \geqslant 1$. Prior investigations of capillary rise in sharp corners have shown that the meniscus altitude increases with time as $t^{1/3}$, a result which is universal, i.e., applies to all corner geometries. The universality of the phenomenon of capillary rise in sharp corners is revisited in this work through the analysis of a partial differential equation for the evolution of a liquid column rising into power-law-shaped corners, which is derived using lubrication theory. Despite the lack of geometric similarity of the liquid column cross-section for $n > 1$, there exists a scaling and a similarity transformation that are independent of c_i and n, which gives rise to the universal $t^{1/3}$ power-law for capillary rise. However, the prefactor, which corresponds to the tip altitude of the self-similar solution, is a function of n, and it is shown to be bounded and monotonically decreasing as $n \to \infty$. Accordingly, the profile of the interface radius as a function of altitude is also independent of c_i and exhibits slight variations with n. Theoretical results are compared against experimental measurements of the time evolution of the tip altitude and of profiles of the interface radius as a function of altitude.

Key words: capillary flows, lubrication theory

1. Introduction

The invasion of a wetting liquid against gravity into a narrow vertical conduit, called capillary rise, is a classical illustration of the effects of capillarity (de Gennes *et al.* 2004). Historically, the phenomenon was a recurring subject of experimentation and speculation, e.g., Hooke (1661), Hauksbee (1706), Jurin (1717), and Laplace (1806), before it was finally attributed to the capillary pressure that arises due to the curvature induced by the contact angle formed by the liquid with the interior surface of the conduit. A viscous liquid driven by capillary effects into a tube of uniform cross-section experiences a constant driving pressure and increasing viscous dissipation, and thus advances diffusively as $t^{1/2}$ (see Bell & Cameron (1906); Lucas (1918); and Washburn (1921)). Different dynamics are observed when the tube cross-section, which affects the capillary pressure and viscous dissipation, varies axially; for example, the advancement of the meniscus into tube with

† Email address for correspondence: kitw@princeton.edu
‡ Email address for correspondence: hastone@princeton.edu

an expanding conical geometry exhibits a $t^{1/4}$ power-law for the meniscus position as a function of time (Reyssat *et al.* 2008).

Flow into open channel geometries differs from flow into closed conduits due to the replacement of a solid boundary by a free interface. The geometry of the flow conduit is no longer fixed, and consequently the curvature of the liquid-air interface, the cross-sectional area, and flow rate are no longer fully determined by the geometry of the solid surfaces. Instead, these quantities vary both axially and with time. In the simplest cases the flow can be modeled by a one-dimensional partial differential equation(PDE). For example, analyses of low-Reynolds-number, unidirectional flow in a sharp triangular corner have been based on the Poisson equation, e.g., Ayyaswamy *et al.* (1974) and Ransohoff & Radke (1988), and the continuity equation relating the axial derivative of flow rate to the time derivative of the cross-sectional area of the conduit then is used to obtain the dynamics, e.g., Lenormand & Zarcone (1984). For cases in which the geometry of the conduit changes with time due to elastocapillary deformations, additional power laws for capillary rise have been identified by Duprat *et al.* (2011) and Di *et al.* (2016).

When a liquid partially filling a triangular corner of interior angle θ_i has a contact angle θ with the adjacent solid walls such that $\theta < (\pi - \theta_i)/2$ (the condition identified by Concus & Finn (1969)), the liquid spontaneously spreads along the corner due to capillarity. For such flows in the absence of gravity, Romero & Yost (1996) and Weislogel & Lichter (1998) analyze the dynamics and identify a similarity solution, which reveals that the meniscus advances as $t^{1/2}$. Warren (2004) identifies different power laws for the spreading of a liquid drop of fixed volume into triangular corner. When the Concus-Finn condition is satisfied, liquid will rise in triangular corners against gravity and approach a hyperbolic equilibrium profile, as originally documented by Taylor (1710) and Hauksbee (1712). Under such circumstances, the tip of the liquid in the corner rises to a theoretically infinite height as $t^{1/3}$ according to a similarity transformation presented by Tang & Tang (1994) and Higuera *et al.* (2008). This power law for capillary rise applies to corners whose shapes are described by arbitrary power-laws $h(x) \propto x^n$, with $n \geqslant 1$, and not just to corners with straight walls ($n = 1$, linear corners), as shown experimentally and argued theoretically by Ponomarenko *et al.* (2011). The universality of this power law was later corroborated by Zhou & Doi (2020) using a PDE derived using the Onsager principle to describe capillary rise into symmetric power-law-shaped corners. Table 1 summarizes the contributions of prior investigations to the understanding of the dynamics of capillary rise in sharp power-law corners.

The initial study of capillary flow in sharp corners by Tang & Tang (1994) was motivated by the practical need to eliminate air bubbles when filling thin tubes, and since then there has been continued interest in the design of both open and closed channels with sharp interior corners to leverage capillary action for precise flow control, e.g., Weislogel & Lichter (1998); Gurumurthy *et al.* (2018); Berthier *et al.* (2019). Studies of capillary flow in confined geometries also aid in the understanding of imbibition in porous media, e.g., Cai *et al.* (2022), and wicking in textiles, e.g., Duprat (2022), which are often characterized by irregularly shaped conduits with a wide range of length scales.

Our aim is to present a derivation using the lubrication approximation of a model of capillary rise in power-law-shaped corners, discuss how self-similarity arises in the phenomenon, and highlight those aspects of the phenomenon that are universal, i.e., independent of the corner geometry, while pointing out those that are not. The paper is organized as follows. In section 2, we describe the geometry of the corner and of the liquid cross-section in horizontal planes. In section 3, we introduce equations that model the flow of a liquid in a narrow channel, and we specialize the equations for the case of capillary rise in section 4. In section 5, we scale variables to render the problem

Reference	Equation	Rate of Rise	Column Geometry
Tang and Tang (1994)	$n = 1$	n/a	n/a
Higuera et al. (2008)	$n = 1$	Exp, Num: $n = 1$	Exp, Num: $n = 1$
Ponomarenko et al. (2011)	n/a	Exp: $n = 1, 2, 3$	n/a
Zhou and Doi (2020)	$n \geqslant 1$ (symmetric)	Num: $n = 1, 2$	Num: $n = 1, 2$
Current Work	$n \geqslant 1$ (generalized)	Exp: $n = 2$	Exp: $n = 2$

TABLE 1. Contributions to the understanding of the universality of capillary rise of a liquid into a sharp corner whose geometry is described by a power-law $h(x) \propto x^n$. In the references listed in this table, the self-similarity of the phenomenon and the $t^{1/3}$ rate of rise of the meniscus are reported. It is indicated whether the reference presented a time evolution equation describing capillary rise in a corner, and whether confirmation of the power-law for capillary rise and the shape of the liquid column were provided. The powers n of each of the contributions are listed, in addition to whether those contributions consisted of experimental measurements (Exp) or numerical results (Num) obtained by solving the governing PDE.

dimensionless, present a similarity transformation that reduces the PDE to an ordinary differential equation (ODE), and briefly discuss the universal and self-similar aspects of the problem. The time evolution of the rising meniscus at early times is modelled in section 6. Section 7 describes the experimental set-up and compares experimental measurements with theoretical predictions. Section 8 concludes the paper.

2. Geometry

2.1. *Power-law corners*

We consider the flow of a liquid into a sharp corner created by two surfaces of possibly different geometry. The surfaces are in contact along the z-axis, which is oriented such that the acceleration of gravity is $-g\mathbf{e}_z$, as depicted in figure 1(a). A schematic of the horizontal cross-sectional geometry is shown in figure 1(b). In the cross section, the surfaces contact at the origin, and their locations are given by

$$h_i(x) = c_i x^n, \qquad i = 1, 2 \qquad n \geqslant 1, \tag{2.1}$$

where n is a real number greater than or equal to one, and the geometric parameters c_i have dimensions of $[\text{Length}]^{-(n-1)}$. We impose the condition $c_2 > c_1$, where the inequality is necessary so that the surfaces do not coincide but the c_i may have the same sign. The thickness of the gap formed by the surfaces is

$$h(x) = h_2(x) - h_1(x) = cx^n, \tag{2.2}$$

where $c = c_2 - c_1$.

Before moving forward, we discuss the applicability of this simple corner geometry, i.e., corners formed by power-law surfaces with a single exponent n, to understanding corners with more varied and complex geometries. One may consider the case in which each surface has a different power, $h_i(x) = c_i x^{n_i}$, e.g., with $n_2 > n_1$. However, this case reduces to $h(x) = h_1(x) = c_1 x^{n_1}$ as $x \to 0$ since $x^{n_2} \ll x^{n_1}$. Furthermore, any arbitrary (smooth) surface profile may be approximated by a Taylor series expansion near $x = 0$,

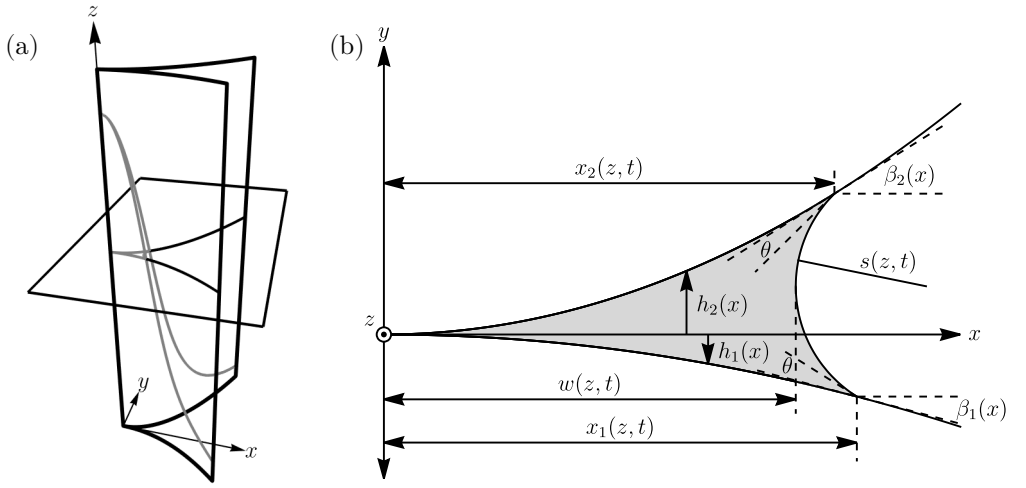

FIGURE 1. Geometry of a power-law corner. (a) Fluid column in the gap formed by two surfaces which meet at vertical line. Gray lines indicate the liquid-solid and liquid-air interfaces. (b) Diagram of a planar cross-section. The corner is located at the origin and it is formed by two surfaces which are located at $h_2(x)$ and $h_1(x)$. The width of the liquid column is $w(z,t)$ and the radius of the liquid-air interface is $s(z,t)$.

which yields a power series. Taking the limit as we approach the corner, we may keep only the leading-order term and thus use a power law to describe the surface geometry. Therefore, we focus our investigations on power-law corners with a single exponent, $n_1 = n_2 = n$, so that we may capture the essential features of the phenomenon while maintaining brevity.

2.2. *Scaling of the dimensions of the liquid cross-section*

In this section, we examine the geometry of the liquid cross-section to identify scaling relationships between its various geometrical descriptors. The width of the column $w(z,t)$ is the minimal value of x of the liquid-air interface, and it is a function of the altitude z (figure 1). The liquid-air interface in the cross-section can assumed to be a circular arc with radius $s(z,t)$. The use and justification of this assumption in the context of capillary rise will be discussed in greater detail in section 4. We anticipate that the liquid column is long and narrow such that the triple line at which the liquid, solid, and air meet is nearly parallel to the z-axis. Therefore, the angle made by the liquid-air interface and the solid surface in the horizontal cross-section is approximated to be the equilibrium contact angle θ of the liquid, which is assumed to be constant.

In the remainder of this section, we will identify the relationship between the interface radius $s(z,t)$, the width $w(z,t)$, and the equilibrium contact angle θ. In particular, we show below that, in certain limits, the radius and width scale as

$$2s(z,t)\cos\theta \sim cw^n(z,t) = h(w(z,t)) \quad \text{or} \quad w(z,t) \sim [2c^{-1}s(z,t)\cos\theta]^{1/n} \quad (n \geqslant 1) \tag{2.3}$$

and $s(z,t) \ll w(z,t)$, which will enable the use of lubrication theory in section 3.

By defining the horizontal positions of the triple lines on the upper and lower surfaces

as $x_2(z,t)$ and $x_1(z,t)$, respectively (see figure 1(b)), we find that

$$x_2(z,t) = w(z,t) + s(z,t)[1 - \sin(\theta + \beta_2(x_2(z,t)))] \tag{2.4a}$$

$$x_1(z,t) = w(z,t) + s(z,t)[1 - \sin(\theta - \beta_1(x_1(z,t)))], \tag{2.4b}$$

where $\beta_i(x) = \tan^{-1}(h_i'(x))$, with $h_i'(x) = \mathrm{d}h_i/\mathrm{d}x$, are the angles measured from the x-axis to the lines tangent to the solid surfaces. Then, by defining the center of the circular arc of the interface as $(x_c(z,t), y_c(z,t))$, we can write

$$y_c(z,t) + s(z,t)\cos(\theta + \beta_2(x_2(z,t))) = h_2(x_2(z,t)) \tag{2.5a}$$

$$y_c(z,t) - s(z,t)\cos(\theta - \beta_1(x_1(z,t))) = h_1(x_1(z,t)). \tag{2.5b}$$

Subtracting the two preceding equations yields the geometrical relationship

$$s(z,t)[\cos(\theta + \beta_2(x_2(z,t))) + \cos(\theta - \beta_1(x_1(z,t)))] = h_2(x_2(z,t)) - h_1(x_1(z,t)). \tag{2.6}$$

For the case $n = 1$, in which case c is dimensionless, we can take the xz-plane to be the symmetry plane of the corner without loss of generality such that $h_2'(x) = -h_1'(x) = c/2$, $\beta_2(x) = -\beta_1(x) = \tan^{-1}(c/2)$ and

$$x_1(z,t) = x_2(z,t) = w(z,t) + s(z,t)\left[1 - \sin\left(\theta + \tan^{-1}\frac{c}{2}\right)\right]. \tag{2.7}$$

Then, (2.6) becomes

$$2s(z,t)\cos\left(\theta + \tan^{-1}\frac{c}{2}\right) = h\left(w(z,t) + s(z,t)\left[1 - \sin\left(\theta + \tan^{-1}\frac{c}{2}\right)\right]\right). \tag{2.8}$$

By using the definition in (2.2), we obtain

$$2s(z,t)\cos\left(\theta + \tan^{-1}\frac{c}{2}\right) = cw(z,t) + cs(z,t)\left[1 - \sin\left(\theta + \tan^{-1}\frac{c}{2}\right)\right]. \tag{2.9}$$

Rearranging and considering the limit $c \ll 1$, we find

$$2s(z,t)\cos\theta \sim cw(z,t) = h(w(z,t)) \quad \text{or} \quad w(z,t) \sim 2c^{-1}s(z,t)\cos\theta \qquad (n = 1). \tag{2.10}$$

For the case $n > 1$, the surfaces are tangent to the xz-plane at $x = 0$ and the $\lim_{x\to 0}\beta_i(x) = 0$. As $x_i(z,t) \to 0$ for $i = 1, 2$, we find that $x_2(z,t) \sim x_1(z,t) \sim w(z,t) + s(z,t)(1 - \sin\theta)$ and (2.6) simplifies to

$$2s(z,t)\cos\theta \sim h(w(z,t) + s(z,t)(1 - \sin\theta)) = c[w(z,t) + s(z,t)(1 - \sin\theta)]^n, \tag{2.11}$$

where the last equality comes from applying the definition of $h(x)$ in (2.2). Since both $s(z,t) \to 0$ and $w(z,t) \to 0$, we anticipate that terms on the right-hand side of (2.11) with powers of $s^2(z,t)$ or greater are insignificant compared to the $s(z,t)$ term on the left, and thus consider the balance

$$2s(z,t)\cos\theta \sim cw^n(z,t) + cnw^{n-1}(z,t)s(z,t)(1 - \sin\theta)). \tag{2.12}$$

By rearranging terms, we find that in the limit $cnw^{n-1}(z,t) \ll 1$,

$$2s(z,t)\cos\theta \sim cw^n(z,t) = h(w(z,t)) \quad \text{or} \quad w(z,t) \sim [2c^{-1}s(z,t)\cos\theta]^{1/n} \quad (n > 1). \tag{2.13}$$

Therefore, in the limit as $x_i(z,t) \to 0$ for $i = 1, 2$, $s(z,t)/w(z,t) \to 0$. Due to the results (2.10) obtained for $n = 1$ and (2.13) for $n > 1$, we may use the relation in (2.3) stated at the start of this section for $n \geqslant 1$ when $cnw^{n-1}(z,t) \ll 1$. In the $n = 1$ case, certain

conditions on the corner geometry (i.e., a small interior angle) must be satisfied. In the $n > 1$ case, c may vary, but for a given value of c we require the dimension of the liquid cross-section to be sufficiently small.

The results derived in this section may be understood through the context of geometric similarity. When two shapes are geometrically similar, corresponding angles and dimensionless ratios between linear dimensions are identical, so that the shapes are scaled versions of each other. Geometric similarity of the liquid cross-sections holds only for $n = 1$. When $n > 1$, $s(z,t)$ and $w(z,t)$ are not directly proportional (see (2.3)), and the ratio $s(z,t)/w(z,t) \to 0$ as the cross-section shrinks to a point. Geometric similarity is also closely tied to the nature of the constant parameters c_i (and c). When $n = 1$, the cross-sections are geometrically similar because the c_i, which are dimensionless descriptors of the geometry, are constant. However, when $n > 1$, the definition of geometric similarity is no longer met because there are constant quantities $c_i^{-1/(n-1)}$ with units of [Length], which leads to dimensionless parameters that vary with the size of the cross-section. Perhaps surprisingly, the introduction of parameters c_i with physical dimensions when $n > 1$ does not preclude the presence of self-similarity in the phenomenon of capillary rise in sharp corners. This result will be discussed in greater detail in section 5.

Finally, we note that by assuming a cross-section of the form in figure 1(b), we implicitly assume that, if the liquid does not extend to $z \to \infty$, the location of the maximum height of the fluid is located on the z-axis ($x = y = 0$), where the two surfaces make contact. However, this is not necessarily true at early times. Work by Higuera *et al.* (2008) and by Ponomarenko *et al.* (2011) show that in the initial stages of capillary rise into a sharp corner, the maximum meniscus altitude is located at some finite x. Higuera *et al.* (2008) develop a model using lubrication theory which reveals that in a linear corner the location of maximum altitude approaches $x = 0$ as $t^{-1/3}$. Ponomarenko *et al.* (2011) use an organ model and find that in corners of general geometry the effective radius of the leading meniscus decreases as $t^{-1/3}$. Given the scaling (2.3) between the interface radius and the width, the location of the maximum altitude is expected to approach the corner as $t^{-1/3n}$, as we discuss more below. Experiments and numerical simulations performed by Higuera *et al.* (2008) find that the location of the maximum is effectively located at $x = 0$ for long times. Therefore, the geometric description of the liquid column given in this section is appropriate when considering the dynamics of capillary rise in a sharp corner at long times when the liquid has assumed a long and narrow geometry. Capillary rise at early times is considered separately. A model based on the work of Higuera *et al.* (2008) is developed for corners with $n \geqslant 1$ in section 6, where we show this $t^{-1/3n}$ power law.

3. Flow in a narrow open channel

In this section, we derive the equation governing the flow of a liquid into a sharp corner. We consider the case in which the liquid occupies a long and narrow space, in particular with $L_y \ll L_x \ll L_z$, where L_x, L_y, and L_z represent the characteristic length scales of velocity variations in their respective directions. The ratios of the characteristic length scales in the cross-sectional plane with that in the primary direction of flow are small, $L_x/L_z \ll 1$ and $L_y/L_z \ll 1$. Thus, we may apply the lubrication approximation, in which we consider the flow to be approximately unidirectional, $\mathbf{u} = u_z(x,y,z,t)\mathbf{e}_z$ and pressure gradients in the xy-plane to be negligible compared to those in the z-direction. Thus, the pressure $p = p(z,t)$ responsible for flow in the channel is approximately a function of z alone (i.e., independent of x and y) and time, t. Such use of lubrication theory is standard in the modeling of many long and narrow flows, such as capillary flow in sharp

corners, e.g., Tang & Tang (1994), Weislogel & Lichter (1998), Higuera *et al.* (2008), Zhou & Doi (2020), etc.

The corner is an open channel, meaning that the liquid flowing in it is not entirely confined by solid surfaces. As a result, the cross-sectional area of the liquid column is a function of both z and t due to the evolution with time of the liquid-air interfaces that comprise the remainder of its boundary. As such, the equation of continuity assuming incompressibility is, e.g., Lenormand & Zarcone (1984),

$$\frac{\partial A}{\partial t} = -\frac{\partial Q}{\partial z}, \tag{3.1}$$

where $A(z,t)$ is the area of the liquid cross-section and $Q(z,t)$ is the volumetric flow rate in the axial direction.

A practical constraint for problems involving flow into a corner from a reservoir is that the volume of liquid in the column is finite for finite time, e.g., Romero & Yost (1996) and Weislogel & Lichter (1998),

$$\int_0^\infty A(z,t)\mathrm{d}z < \infty \quad \text{for} \quad 0 \leqslant t < \infty. \tag{3.2}$$

This finite volume condition results in the boundary conditions (5.9) and (5.10) below, which are derived in Appendix B and presented in section 5, for the ODE obtained by applying a similarity transformation to the governing equation (4.6) derived in section 4. The area of the cross-section is found by integrating the height of the gap over the width of the liquid column $w(z,t)$,

$$A(z,t) = \int_0^{w(z,t)} h(x)\mathrm{d}x = \frac{c}{n+1} w^{n+1}(z,t), \tag{3.3}$$

in which higher-order terms due to the curvature of the interface in the xy-plane have been neglected since we consider the limit $s(z,t)/w(z,t) \ll 1$.

The flow rate is calculated by integrating the axial velocity over the area of the liquid cross-section. Due to the separation of length scales, $L_y \ll L_x \ll L_z$, the gradients of the axial velocity in the x- and z-directions are negligible in comparison to that in the y-direction, and we may write for the axial velocity:

$$\frac{\partial^2 u_z}{\partial y^2} = \frac{1}{\mu}\frac{\partial p}{\partial z}, \tag{3.4}$$

where μ is the dynamic viscosity and $p(z,t)$ is the pressure. Lubrication theory was applied in this way in the plane of the cross-section by Zhou & Doi (2020). We impose the no-slip boundary conditions at the bounding surfaces,

$$u_z(x, h_2(x), z, t) = u_z(x, h_1(x), z, t) = 0, \tag{3.5}$$

and find that the velocity profile is parabolic:

$$u_z(x,y,z,t) = -\frac{1}{2\mu}\frac{\partial p}{\partial z}\left[-y^2 + [h_2(x) + h_1(x)]y - h_1(x)h_2(x)\right]. \tag{3.6}$$

The corresponding expression for the velocity distribution given by Zhou & Doi (2020) (see their equation (2.9)) for a symmetric gap is recovered when we set $c_2 = -c_1 = c/2$. The flow rate is calculated by integrating the velocity over the cross-section,

$$Q(z,t) = \int_0^{w(z,t)} \int_{h_1(x)}^{h_2(x)} u_z(x,y,z,t)\mathrm{d}y\mathrm{d}x = -\frac{1}{12\mu}\frac{\partial p}{\partial z}\frac{c^3}{3n+1} w^{3n+1}(z,t). \tag{3.7}$$

Although the velocity field depends on the parameters c_i corresponding to the individual surfaces, the flow rate depends only on the combined geometric parameter c of the gap. Thus, the approximations of the area and the flow rate are unaffected by the asymmetry of the corner and depend only on the total thickness of the gap $h(x)$, a result which may be expected due to the narrow geometries required in the application of lubrication theory.

Making use of (2.3), we can write (3.3) and (3.7) in terms of the interface radius,

$$A(z,t) = \frac{2^{1+1/n}}{n+1} c^{-1/n} [s(z,t)\cos\theta]^{1+1/n} \qquad \text{and} \tag{3.8a}$$

$$Q(z,t) = -\frac{1}{3\mu}\frac{\partial p}{\partial z}\frac{2^{1+1/n}}{3n+1} c^{-1/n} [s(z,t)\cos\theta]^{3+1/n}. \tag{3.8b}$$

Inspecting equations (3.3), (3.7), and (3.8) and knowing that $s \propto cw^n$, we observe that $A \propto ws$ and $Q \propto ws^3$. One may arrive at the scaling of the area by using a reasonable estimate of the area of the cross-section as a product of characteristic length scales in orthogonal directions. The scaling for the flow rate may be expected from analysis of the classical problem of unidirectional viscous flow in a channel with a high-aspect-ratio ($L_y \ll L_x$) rectangular cross-section (Boussinesq 1868). When $n = 1$, $s \propto w$, there is geometric similarity, and the scaling of the area and flow rate may described by a single length scale $A \propto w^2 \propto s^2$ and $Q \propto w^4 \propto s^4$. When $n > 1$, there is no geometric similarity, and both the area and flow rate scale with fractional powers of the linear dimensions. The proper dimensions for both quantities are achieved by the inclusion of the appropriate power of the geometric parameter c characteristic of the corner geometry.

Rewriting the continuity equation (3.1) using the expressions (3.8), we arrive at

$$\frac{\partial}{\partial t}\left[s^{1+1/n}(z,t)\right] = \frac{\cos^2\theta}{3\mu}\frac{n+1}{3n+1}\frac{\partial}{\partial z}\left[s^{1+1/n}(z,t)\frac{\partial p}{\partial z}\right]. \tag{3.9}$$

The finite volume condition becomes

$$\int_0^\infty s^{1+1/n}(z,t)\mathrm{d}z < \infty \qquad \text{for} \qquad 0 \leqslant t < \infty \tag{3.10}$$

which is used to obtain boundary conditions for (3.9) (see Appendix B for detailed derivations) and will be presented later in section 5 (see (5.9) and (5.10)).

In the next section, these equations are specialized for capillary rise by substituting the appropriate expression for the pressure gradient. The relevant boundary condition is also provided.

4. Capillary rise

We examine capillary rise against gravity, or flow due to the Young-Laplace pressure, arising from the curved liquid-air interface and conservative gravitational body forces. As originally noted by Tang & Tang (1994), the flow is driven due to gradients in the modified pressure (Batchelor 1967). Due to the long and narrow geometry of the liquid column, the axial curvature is negligible, and the mean curvature of the interface determined primarily by the curvature in the horizontal cross-section. Since the pressure is constant in the xy-plane, the mean curvature must be the same at every point of the interface in the cross-section. So, the interface in the cross-section is taken to be a circular arc with radius $s(z,t)$, and the modified pressure is

$$p(z,t) = -\frac{\gamma}{s(z,t)} + \rho g z. \tag{4.1}$$

At a given time t, we expect the interface to converge to its equilibrium shape for which the Young-Laplace pressure balances the hydrostatic pressure as we approach the reservoir. Furthermore, at a given altitude z, we expect capillary pressure and hydrostatic pressure to balance at long times. These conditions are expressed as

$$s(z,t) \sim \frac{\ell_{cg}^2}{z} \quad \text{as} \quad z \to 0 \quad \text{or} \quad t \to \infty \tag{4.2}$$

or in terms of the width of the column,

$$w(z,t) \sim \left(\frac{2c^{-1}\ell_{cg}^2 \cos\theta}{z} \right)^{1/n} \quad \text{as} \quad z \to 0 \quad \text{or} \quad t \to \infty \tag{4.3}$$

where $\ell_{cg} = \sqrt{\gamma/\rho g}$ is the capillary length.

Since the radius is a hyperbolic function of the altitude z in (4.2), it is implied that that capillary rise in sharp corners never reaches an equilibrium in the current model. Realistically, capillary rise changes due to other effects such as van der Waals forces, which become important for small enough length scales. We note that the profile of the meniscus is hyperbolic as reported by Hauksbee (1712) only for the case $n = 1$.

In the equilibrium profile (4.3), the first and second derivatives of the width become large as we approach the reservoir. In this limit, the assumptions that the inclinations of the triple lines are insignificant and that the axial curvature of the interface is negligible are invalid. Then, the angle of the liquid-air interface with the solid boundaries would no longer be approximately equal to the equilibrium contact angle, and due to the contributions of the axial curvature to the mean curvature of the interface, (4.2) would no longer hold. Furthermore, the axial curvature would not necessarily be identical everywhere on the interface in the cross-section, which would lead to deviations of the interface from a circular arc.

We may identify conditions for the validity of these assumptions by estimating the inclinations and axial curvature given the equilibrium profile (4.2). The first derivative of the width $\mathrm{d}w/\mathrm{d}z$ can be used to approximate the magnitude of the slope of the triple line, which is thus found to be $O(w/z)$. The axial curvature may approximated by the second derivative of the width,

$$\frac{\mathrm{d}^2 w}{\mathrm{d}z^2} = \frac{n+1}{n^2} \frac{(2c^{-1}\ell_{cg}^2 \cos\theta)^{1/n}}{z^{2+1/n}} = \frac{n+1}{n^2} w^{-1} \left(\frac{w}{z} \right)^2 \tag{4.4}$$

where we have used the equilibrium relation between w and z (4.3). Therefore, the axial curvature and any perturbations to a circular interface of radius $s(z,t)$ are $O((w/z)^2)$. Corrections to the shape and mean curvature of the interface at equilibrium for the $n = 1$ case are provided by Tang & Tang (1994). Corrections for general $n \geqslant 1$ are not included here.

Going forward, we omit the functional dependence of variables for brevity. The axial gradient of the pressure (4.1) is

$$\frac{\partial p}{\partial z} = \frac{\gamma}{s^2}\frac{\partial s}{\partial z} + \rho g = \frac{\gamma}{s^2}\left(\frac{\partial s}{\partial z} + \frac{s^2}{\ell_{cg}^2} \right). \tag{4.5}$$

Using (4.5) in (3.9) we obtain the equation describing capillary rise in a power-law corner:

$$\frac{\partial}{\partial t}\left(s^{1+1/n} \right) = \frac{\gamma \cos^2\theta}{3\mu} \frac{n+1}{3n+1} \frac{\partial}{\partial z}\left[s^{1+1/n} \left(\frac{\partial s}{\partial z} + \frac{s^2}{\ell_{cg}^2} \right) \right]. \tag{4.6}$$

The time evolution equation (4.6) prior to non-dimensionalization may be compared with equation (3.6) of Zhou & Doi (2020), which is an equivalent equation written in terms of the column width (see appendix A) and involves both c and n. We note that with the choice of the interface radius $s(z,t)$ as the dependent variable, equation (4.6) is independent of details of gap geometry aside from the power n in the coefficients: the fractional exponents simplify upon distribution of the derivatives, and the parameter c does not appear. The limited influence of the corner geometry is reminiscent of the initial proposal by Ponomarenko *et al.* (2011) of a universal law for capillary rise in corners and the later observation by Zhou & Doi (2020) that tip dynamics are independent of c. The next section is dedicated to identifying the aspects of capillary rise in sharp corners that are universal and those that are not by analyzing equation (4.6).

5. Scaling and a self-similar solution

5.1. *Scaling*

Equation (4.6) is made dimensionless by scaling lengths and time using

$$\tilde{z} = \frac{z}{\ell_{cg}(\cos\theta)^{1/2}}, \qquad \tilde{s} = \frac{(\cos\theta)^{1/2}s}{\ell_{cg}}, \qquad \text{and} \qquad \tilde{t} = \frac{\gamma(\cos\theta)^{1/2}t}{3\mu\ell_{cg}}. \tag{5.1a,b,c}$$

Due to the absence of c from (4.6), characteristic scales are used here that are independent of c, or alternatively independent of the length scale $c^{-1/(n-1)}$ $(n > 1)$ of the corner geometry. A similar choice of characteristic scales for time and altitude was made by Ponomarenko *et al.* (2011), which reflects the expected universality of the phenomenon. For ease of comparison with other statements of this capillary rise problem, e.g., Higuera *et al.* (2008) and Zhou & Doi (2020), the scaling and similarity transformation for the equivalent expression of (4.6) in terms of the width $w(z,t)$ is given in Appendix A.

Applying the scaling (5.1a,b,c) leads to the equation

$$\frac{\partial}{\partial\tilde{t}}\left(\tilde{s}^{1+1/n}\right) = \frac{n+1}{3n+1}\frac{\partial}{\partial\tilde{z}}\left[\tilde{s}^{1+1/n}\left(\frac{\partial\tilde{s}}{\partial\tilde{z}} + \tilde{s}^2\right)\right], \tag{5.2}$$

subject to the conditions

$$\tilde{s}(\tilde{z},\tilde{t}) \sim \frac{1}{\tilde{z}} \quad \text{as} \quad \tilde{z}\to 0 \quad \text{or} \quad \tilde{t}\to\infty \tag{5.3}$$

and

$$\int_0^\infty \tilde{s}^{1+1/n}\mathrm{d}\tilde{z} < \infty \quad \text{for} \quad 0 \leqslant \tilde{t} < \infty. \tag{5.4}$$

5.2. *Similarity solution*

We observe that the problem described in (5.2), (5.3), and (5.4) is invariant under the one-parameter family of scaling transformations

$$\hat{z} = \chi\tilde{z} \qquad \hat{t} = \chi^3\tilde{t} \qquad \hat{s} = \chi^{-1}\tilde{s}, \tag{5.5a,b,c}$$

thus we know that there is a similarity solution of the form, e.g., Bluman & Kumei (2013) and Debnath (2005),

$$\phi(\eta) = \tilde{t}^{1/3}\tilde{s}(\tilde{z},\tilde{t}) \quad \text{where} \quad \eta = \tilde{t}^{-1/3}\tilde{z}. \tag{5.6}$$

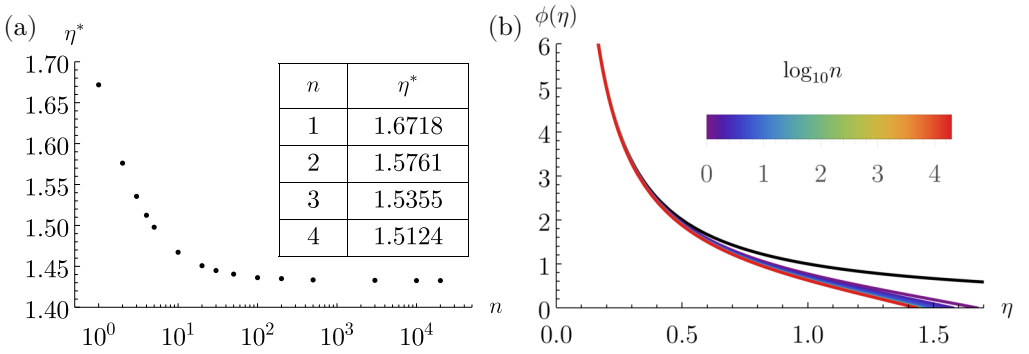

n	η^*
1	1.6718
2	1.5761
3	1.5355
4	1.5124

FIGURE 2. Solutions to the ODE (5.7) (a) The dimensionless tip altitude η^* as a function of n. The values of η^* corresponding to the first few integer n are listed in the inset table. A complete table can be found in appendix C. In the limit $n \to \infty$, $\phi'(\eta^*) \to \eta^* \approx 1.4326$. (b) The function $\phi(\eta)$ obtained by numerically solving the ODE. The condition for hydrostatic equilibrium (5.8*a*), $\phi(\eta) = 1/\eta$, is shown in black.

Applying the transformation produces the ODE

$$-\frac{1}{3}\eta\frac{\mathrm{d}}{\mathrm{d}\eta}\left(\phi^{1+1/n}\right) = \frac{n+1}{3n+1}\frac{\mathrm{d}}{\mathrm{d}\eta}\left[\phi^{1+1/n}\left(\frac{\mathrm{d}\phi}{\mathrm{d}\eta}+\phi^2\right)\right] \tag{5.7}$$

with the conditions

$$\phi(\eta) \sim \frac{1}{\eta} \quad \text{as} \quad \eta \to 0 \qquad \text{and} \tag{5.8a}$$

$$\int_0^\infty \phi(\eta)^{1+1/n}\mathrm{d}\eta < \infty. \tag{5.8b}$$

Following an argument (see Appendix B for details) similar to that presented by Romero & Yost (1996) for capillary flow into a sharp horizontal groove, the inequality in (5.8*b*) can be used to show that the liquid column extends to a finite altitude z^* (or η^* in dimensionless terms) at which the cross-section reduces to a point,

$$\phi(\eta^*) = 0, \tag{5.9}$$

as well as to derive a boundary condition at this location,

$$\phi'(\eta^*) = -\frac{3n+1}{3(n+1)}\eta^*. \tag{5.10}$$

Analogous conditions were also adopted by Weislogel & Lichter (1998). Higuera *et al.* (2008) and Zhou & Doi (2020) derive an equivalent boundary condition expressed in terms of a function approximating the profile of the column near the tip. The ODE (5.7) was solved numerically using (5.8*a*), (5.9), and (5.10) (see Appendix C for details). The dimensionless tip altitude η^* for a series of integer n are plotted in figure 2(a). Figure 2(a) contains an inset table listing the η^* corresponding to the first few values of n, and a complete table is provided in Appendix C. In the limit as $n \to \infty$, the boundary condition (5.10) implies that $\phi'(\eta^*) \to -\eta^*$. By numerically solving the ODE, we find that $\lim_{n\to\infty} \eta^* \approx 1.4326$ (see figure 2(a)). The corresponding solutions $\phi(\eta)$ are plotted in figure 2(b).

5.3. *Self-similarity and universality*

This section briefly discusses the existence of self-similar and universal aspects of capillary rise in sharp corners. In the language of Barenblatt (2003), phenomena are similar if they differ only in the values of their corresponding physical parameters while their corresponding dimensionless parameters are identical. This is the natural generalization of geometric similarity in which dimensionless quantities like angles and length ratios are preserved while a shape is scaled. Furthermore, we say that phenomena are self-similar when there exists a time- or space-dependent scaling of dimensional quantities for which the phenomenon becomes invariant. Self-similar phenomena are characterized by power-law growth and the existence of similarity transformations through which it is possible to reduce the number independent variables and in this case obtain an ODE from a PDE. Self-similarity is often observed in the propagation of persistent singularities, such as the motion of contact lines at the edges of spreading drops, e.g., Eggers & Fontelos (2015). A common feature of self-similar phenomena is universality, since self-similarity is usually observed in the intermediate asymptotic regime in which both initial conditions and the large scale structure of the solution are irrelevant. The term "universal" is used here to refer to features of capillary rise in sharp corners that do not depend on corner geometry, or in other words that are common for all powers n and geometric parameters c.

As discussed in section 2, there is an additional length scale $c^{-1/(n-1)}$ characteristic of the corner geometry when $n > 1$, and the liquid cross-section lacks geometric similarity due to the existence of dimensionless quantities that are not constant as the size of the cross-section is varied. The system also fails to satisfy the definition of physical similarity for the same reason. However, when written in terms of the interface radius, the cross-sectional area and flow rate (3.8) scale with the same power of c, and thus c does not appear in the evolution equation expressed in terms of the interface radius (4.6) even prior to non-dimensionalization. As noted previously, the fractional exponents in (4.6) and (5.2) simplify upon distribution of the derivatives, and information about the corner geometry remains only in the power n in the coefficients. It becomes apparent that there is a similarity transformation (5.6) that is independent of c and n, and so we confirm the universality of $t^{1/3}$ proposed by Ponomarenko *et al.* (2011). That is, the tip altitude advances with the same power of t for all corner geometries:

$$\frac{z^*}{\ell_{cg}(\cos\theta)^{1/2}} = \eta^* \left(\frac{\gamma(\cos\theta)^{1/2} t}{3\mu\ell_{cg}} \right)^{1/3}, \tag{5.11}$$

or

$$\tilde{z}^* = \eta^* \tilde{t}^{1/3}. \tag{5.12}$$

The scaling of the tip altitude with time in (5.11) is equivalent to the result in Zhou & Doi (2020) (see their equation (3.25)) up to factors of n despite differences in the choices of characteristic lengths in the intervening scaling step and in the form of the ODE obtained by similarity transformation. In (5.11) and (5.12), the constant c is absent. However, due to the dependence of the prefactor and dimensionless tip altitude η^* on n, the rate of capillary rise is not truly universal. The prefactor η^* of the power law varies with n because n appears in the coefficients of the nonlinear evolution equation (4.6) and in the boundary condition (5.10). The quantity η^* decreases monotonically with the power n, and its value is bounded between approximately 1.6718 and 1.4350 for $1 \leqslant n < \infty$ (see figure 2(a)). Zhou & Doi (2020) also report that variations in the prefactor are small based on values obtained up to $n = 5$, which are tabulated in their table 1.

In summary, we anticipate that capillary rise proceeds as $t^{1/3}$ for all c and n, and that the rates of capillary rise in corners characterized by the same power n are the same

regardless of the values of c. Furthermore, we can identify another feature shared by liquid columns rising in corners. For a given n, the profiles of the interface radius s as a function of the axial coordinate z are identical regardless of the value of c, and they all share the same self-similar profile. Experimental data is presented in section 7 that illustrate these results.

In the next section, we examine the early stages of capillary rise. Power laws for the evolution of geometric features of the meniscus are identified that depend differently on the geometry of the corner than those presented for capillary rise at late times in which the liquid geometry is long and narrow. The following result suggests that the corner geometry affects the dynamics of capillary rise in ways that are not always straightforward.

6. Capillary rise at early times

In this section, we examine the early stages of the capillary rise phenomenon using a formulation of the problem in terms of the altitude of the meniscus $Z(x,t)$. The developments in this section follow Higuera *et al.* (2008) who reported an analogous calculation for linear corners. It is found that the maximum altitude of the meniscus does not coincide with the line of contact of the surfaces forming the corner. This problem also admits a similarity solution, which reveals the rates at which the maximum altitude of the meniscus increases and at which the location of this maximum approaches the corner.

6.1. *Model*

First, by applying lubrication theory and making use of the separation of scales $L_y \ll L_x$ and $L_y \ll L_z$, we write the velocities averaged over the gap height

$$(u_x, u_z) = -\frac{h^2(x)}{\mu}\left(\frac{\partial p}{\partial x}, \frac{\partial p}{\partial z}\right) \qquad 0 < z < Z(x,t), \quad x > 0 \tag{6.1}$$

where $p(x,z,t)$ is the pressure driving the flow. The pressure is approximately constant in the y-direction as a result of the geometry, and the velocity u_y is negligible, $u_y/u_x \ll 1$ and $u_y/u_z \ll 1$. The corresponding flux in each direction is

$$(q_x, q_z) = -\frac{h^3(x)}{\mu}\left(\frac{\partial p}{\partial x}, \frac{\partial p}{\partial z}\right) \qquad 0 < z < Z(x,t), \quad x > 0. \tag{6.2}$$

Using (2.2), we substitute for the gap height (x)

$$(u_x, u_z) = -\frac{c^2 x^{2n}}{\mu}\left(\frac{\partial p}{\partial x}, \frac{\partial p}{\partial z}\right) \qquad 0 < z < Z(x,t), \quad x > 0 \tag{6.3}$$

$$(q_x, q_z) = -\frac{c^3 x^{3n}}{\mu}\left(\frac{\partial p}{\partial x}, \frac{\partial p}{\partial z}\right) \qquad 0 < z < Z(x,t), \quad x > 0. \tag{6.4}$$

For an incompressible flow, mass conservation requires $\partial q_x/\partial x + \partial q_z/\partial z = 0$, or

$$\frac{\partial}{\partial x}\left(x^{3n}\frac{\partial p}{\partial x}\right) + x^{3n}\frac{\partial^2 p}{\partial z^2} = 0 \qquad 0 < z < Z(x,t). \tag{6.5}$$

At the edge of the corner where the surfaces contact, we expect the velocity and flux to vanish, or equivalently

$$\frac{\partial p}{\partial x} \to 0 \qquad \text{as} \qquad x \to 0. \tag{6.6}$$

The reference pressure is

$$p(x, z = 0, t) = 0, \tag{6.7}$$

and a pressure boundary condition holds at the interface:

$$p(x, z = Z(x,t), t) = -\frac{2\gamma\cos\theta}{cx^n} + \rho g Z(x,t) \tag{6.8}$$

where it has been assumed that axial contributions to mean curvature are negligible and that the interface is approximately circular in horizontal cross-sections, and the definition (2.2) and asymptotic relation (2.3) have been applied. We assume that the meniscus is a material surface that travels with the average velocity, $\mathrm{D}Z/\mathrm{D}t = u_z$, in which case

$$\frac{\partial Z}{\partial t} - \frac{c^2 x^{2n}}{\mu}\frac{\partial p}{\partial x}\frac{\partial Z}{\partial x} + \frac{c^2 x^{2n}}{\mu}\frac{\partial p}{\partial z} = 0 \qquad \text{at} \quad z = Z(x,t). \tag{6.9}$$

If we begin with the initial condition

$$Z(x, t = 0) = 0, \tag{6.10}$$

then the characteristic scale in the vertical direction is small compared to that in the horizontal direction, $L_z \ll L_x$ and we may use lubrication theory to simplify (6.5) and (6.9) to

$$\frac{\partial^2 p}{\partial z^2} = 0 \qquad 0 < z < Z(x,t), \quad x > 0, \quad \text{and} \tag{6.11}$$

$$\frac{\partial Z}{\partial t} + \frac{c^2 x^{2n}}{\mu}\frac{\partial p}{\partial z} = 0 \qquad \text{at} \quad z = Z(x,t). \tag{6.12}$$

6.2. *Scaling and Similarity Solution*

Scaling the lengths by

$$(\tilde{z}, \tilde{Z}) = \frac{(z, Z)}{\ell_{cg}(\cos\theta)^{1/2}} \qquad \text{and} \qquad \tilde{x} = \frac{x}{\left[2c^{-1}\ell_{cg}(\cos\theta)^{1/2}\right]^{1/n}} \tag{6.13a,b}$$

and pressure and time by

$$\tilde{p} = \frac{p}{\rho g \ell_{cg}(\cos\theta)^{1/2}} \qquad \text{and} \qquad \tilde{t} = \frac{\gamma(\cos\theta)^{1/2} t}{3\mu\ell_{cg}}, \tag{6.14a,b}$$

we obtain the system

$$\frac{\partial^2 \tilde{p}}{\partial \tilde{z}^2} = 0 \qquad 0 < \tilde{z} < \tilde{Z}(\tilde{x}, \tilde{t}), \quad \tilde{x} > 0 \tag{6.15a}$$

$$\tilde{p}(\tilde{x}, \tilde{z} = 0, \tilde{t}) = 0 \tag{6.15b}$$

$$\tilde{p}(\tilde{x}, \tilde{z} = \tilde{Z}(\tilde{x}, \tilde{t}), \tilde{t}) = -\frac{1}{\tilde{x}^n} + \tilde{Z}(\tilde{x}, \tilde{t}), \tag{6.15c}$$

$$\frac{\partial \tilde{Z}}{\partial \tilde{t}} + 12\tilde{x}^{2n}\frac{\partial \tilde{p}}{\partial \tilde{z}} = 0 \qquad \text{at} \quad \tilde{z} = \tilde{Z}(\tilde{x}, \tilde{t}), \quad \text{and} \tag{6.15d}$$

$$\tilde{Z}(\tilde{x}, \tilde{t} = 0) = 0. \tag{6.15e}$$

Solving (6.15a) with (6.15b) and (6.15c) yields the solution for the pressure

$$\tilde{p}(\tilde{x}, \tilde{z}, \tilde{t}) = \frac{\tilde{z}}{\tilde{Z}(\tilde{x}, \tilde{t})}\left(\tilde{Z}(\tilde{x}, \tilde{t}) - \frac{1}{\tilde{x}^n}\right). \tag{6.16}$$

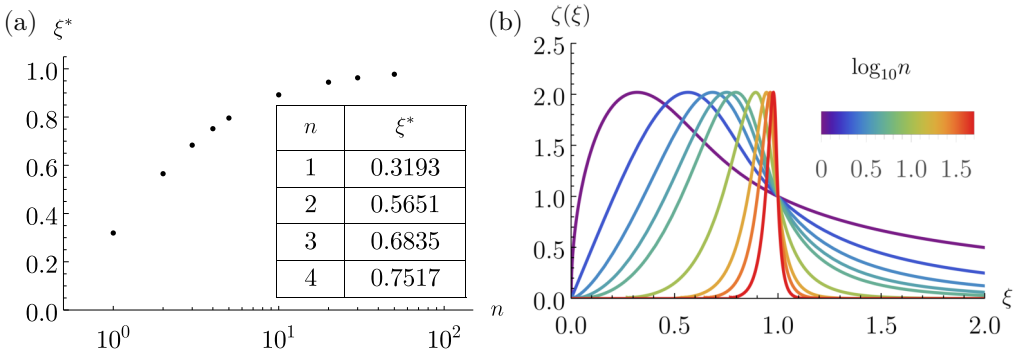

n	ξ^*
1	0.3193
2	0.5651
3	0.6835
4	0.7517

FIGURE 3. Similarity solution for capillary rise at early times. (a) Locations ξ^* of the maximum of the function $\zeta(\xi)$ as a function of n. (b) Profiles of $\zeta(\xi)$ for different n.

Substituting the expression for the pressure (6.16) into (6.15*d*), we obtain

$$\frac{\partial \tilde{Z}}{\partial t} = 12\tilde{x}^n \left(\frac{1 - \tilde{Z}(\tilde{x},\tilde{t})\tilde{x}^n}{\tilde{Z}(\tilde{x},\tilde{t})} \right), \tag{6.17}$$

which can be solved with the initial condition (6.15*e*) to find

$$-\tilde{x}^n \tilde{Z}(\tilde{x},\tilde{t}) - \ln[1 - \tilde{x}^n \tilde{Z}(\tilde{x},\tilde{t})] = 12\tilde{x}^{3n}\tilde{t}. \tag{6.18}$$

We observe that (6.18) is invariant under the one parameter family of scaling transformations

$$\hat{x} = \chi\tilde{x} \qquad \hat{t} = \chi^{-3n}\tilde{t} \qquad \hat{Z} = \chi^{-n}\tilde{Z}. \tag{6.19a,b,c}$$

Therefore, there is a similarity transformation

$$\zeta(\xi) = \tilde{t}^{-1/3}\tilde{Z}(\tilde{x},\tilde{t}) \quad \text{where} \quad \xi = \tilde{t}^{1/3n}\tilde{x} \tag{6.20}$$

through which we obtain

$$-\xi^n\zeta - \ln(1 - \xi^n\zeta) = 12\xi^{3n}. \tag{6.21}$$

The solution for $\zeta(\xi)$ can be written using the Lambert W-function

$$\zeta(\xi) = \xi^{-n}\left[1 + W\left(-e^{-1-12\xi^{3n}}\right)\right]. \tag{6.22}$$

6.3. *Evolution of the maximum meniscus altitude*

Taking the derivative of (6.21) with respect to ξ, and setting $\zeta'(\xi) = 0$, we find that there is a maximum ζ^* located at ξ^* such that

$$(\xi^*)^n\zeta^*\left(\frac{1}{1 - (\xi^*)^n\zeta^*} - 1\right) = 36(\xi^*)^{3n}. \tag{6.23}$$

The location ξ^* of the maximum is shown in figure 3(a), and the corresponding solutions to (6.21) are shown in figure 3(b). Also, it is possible to examine (6.21) to determine how the location and value of the maximum depends on the power n.

It can be shown that $\zeta^* \approx 2.0200$ for all n and that $\xi^* \to 1$ as $n \to \infty$. By defining $\chi = \xi^n\zeta$, we can write (6.21) and (6.23) as

$$-3\chi^* - 3\ln(1 - \chi^*) = 36(\xi^*)^{3n} \tag{6.24a}$$

and

$$\chi^* \left(\frac{1}{1-\chi^*} - 1 \right) = 36(\xi^*)^{3n}. \tag{6.24b}$$

In writing (6.24*a*), we have used the fact that if (6.21) applies for all ξ and $\zeta(\xi)$, it must be true at ξ^* and ζ^*. Then, noting that the expressions on the right sides of (6.24*a*) and (6.24*b*) are identical, we set the left sides equal,

$$\chi^* \left(\frac{1}{1-\chi^*} - 1 \right) = -3\chi^* - 3\ln(1-\chi^*) \tag{6.25}$$

and find that $\chi^* \approx 0.6450$. Then, we use (6.24*a*) or (6.24*b*) to solve for $(\xi^*)^n$, and we conclude that $(\xi^*)^n \approx 0.3193$. $(\xi^*)^n$ is a constant, so $\xi^* \to 1$ as $n \to \infty$. Furthermore, by using the definition of χ, we find that $\zeta^* = (\xi^*)^{-n}\chi^* \approx 2.0200$, which is constant for all n. We observe these features in figure 3(b).

Due to (6.20), we find that the location of the maximum moves towards $\tilde{x} = 0$ as

$$\tilde{x}^* = \xi^* \tilde{t}^{-1/3n}, \tag{6.26}$$

where the prefactor ξ^* is a function of n. Using physical quantities,

$$\frac{x^*}{\left[2c^{-1}\ell_{cg}(\cos\theta)^{1/2}\right]^{1/n}} = \xi^* \left(\frac{\gamma(\cos\theta)^{1/2} t}{3\mu\ell_{cg}} \right)^{-1/3n}. \tag{6.27}$$

The maximum meniscus altitude increases as

$$\tilde{Z}^* = \zeta^* \tilde{t}^{1/3}. \tag{6.28}$$

or

$$\frac{Z^*}{\ell_{cg}(\cos\theta)^{1/2}} = \zeta^* \left(\frac{\gamma(\cos\theta)^{1/2} t}{3\mu\ell_{cg}} \right)^{1/3}. \tag{6.29}$$

Therefore, in the early stages of capillary rise, we expect the rate at which the meniscus rises (6.29) to be universal, that is, independent of c and n. However, the rate at which the location of the maximum altitude approaches the corner (6.27) depends on both c and n.

7. Experiments

7.1. *Methods*

Experiments were conducted in order to measure the rate of capillary rise at late times as well as the shape of the liquid column in a quadratic corner ($n = 2$), which was formed by the contact of a cylinder and a flat plate. A closed contour centered at $x = 0, y = \pm b_i$ with geometry described by (Stone 2005)

$$x^m + y_i^m = b_i^m \tag{7.1}$$

where m is a positive, even integer and $y_i = y \mp b_i$ creates a surface at

$$h_i(x) \sim \pm c_i x^n \tag{7.2}$$

where $n = m$ and

$$c_i = \pm \frac{1}{m b_i^{m-1}}. \tag{7.3}$$

Corners were created by pressing a flat plate ($b_1 = \infty$) to a circular cylindrical tube ($m = 2$) of radius $b_2 = b$, both made of glass, so that the corner is formed by surfaces at

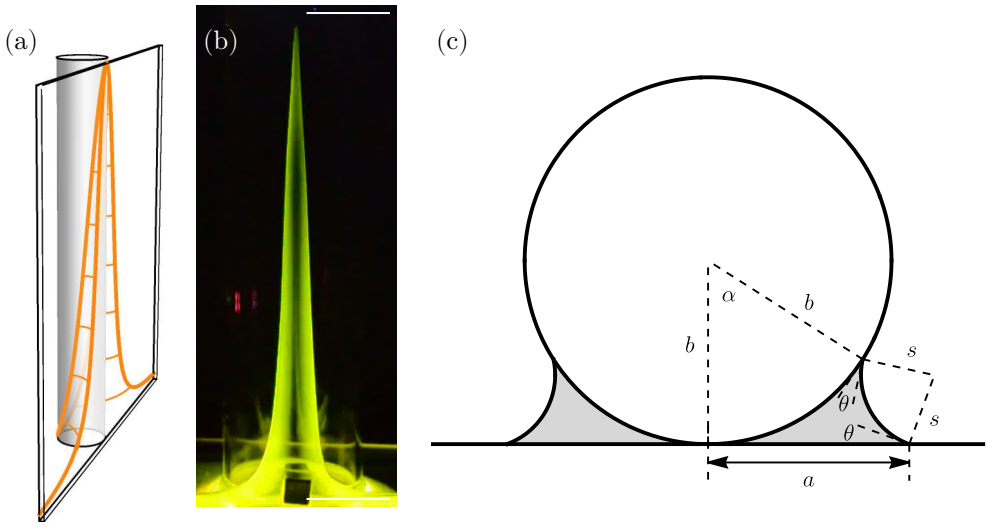

FIGURE 4. Rise of a liquid column in the corner formed by a cylinder and a plate ($n = m = 2$). (a) Graphical rendering of fluid interface viewed from an angle. (b) Image of the liquid column from an experiment with a view orthogonal to the plate. Scale bar is 10 mm. (c) Geometry of a horizontal cross-section of a liquid column between a cylinder and plate.

	Dynamic Viscosity	Density	Surface Tension	Capillary Length	Contact Angle
	μ [mPa s]	ρ [g/mL]	γ [mN/m]	ℓ_{cg} [mm]	θ [°]
Silicone Oil	16.7	0.950	19.2	1.44	0
Mineral Oil	28.6	0.838	27.1	1.82	20

TABLE 2. Relevant properties of the liquids used in experiments.

$h_2(x) \sim cx^2$ with $c = 1/2b$ and $h_1(x) = 0$. Experiments were performed for two different cylinder radii, $b = 4$ mm and $b = 9$ mm. Figure 4(a) shows a schematic of the liquid column rising in such a configuration. Pairs of magnets placed at two axial locations were used to hold the tube and plate in contact. Prior to the experiments, the glass was cleaned using ethanol and distilled water.

Experiments were performed using silicone oil (Sigma Aldrich, Product Number 378348) and mineral oil (Sigma Aldrich, Product Number 330779), whose properties are listed in table 2. The oils were dyed using fluorescent automotive dye (The Dow Chemical Company, Fluorescent Yellow 131SC) at concentrations of 5 μL per 20 mL for mineral oil and 20 μL per 20 mL for silicone oil. For imaging, the liquid was illuminated with 365 nm UV light. An experimental image of the illuminated liquid column is shown in figure 4(b). Due to the use of fluorescent dye, the pixels corresponding to the liquid have much greater intensity values compared to those corresponding to the background. The tip altitude is identified by locating the steep gradient in pixel intensity between the background and the liquid.

Experiments were recorded using a DSLR camera (Nikon, D5100) oriented so that the focal plane was parallel with the plate. Videos were acquired at 30 frames per second

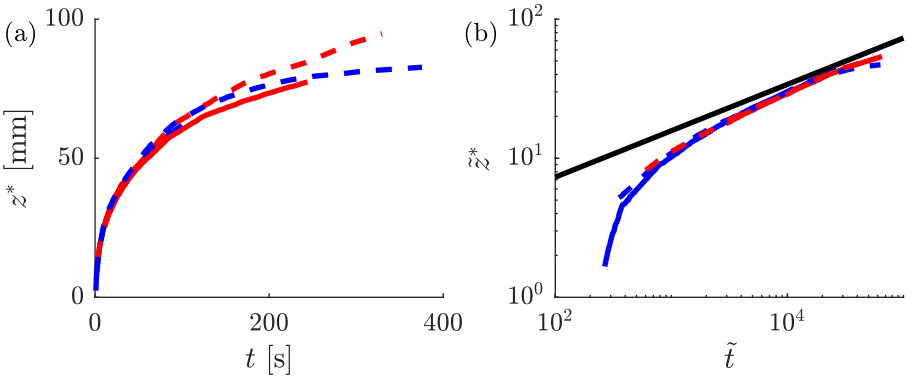

FIGURE 5. Location of the tip of the liquid column as a function of time. Data are shown for $b = 9$ mm in red and $b = 4$ mm in blue. Solid lines indicate data for silicone oil and dashed lines indicate data for mineral oil. (a) With dimensions and plotted on linear axes. (b) Non-dimensionalized and plotted on log-log axes. The function (5.12) with the value of $\eta^* = 1.5761$ (for $n = 2$) is shown as a solid black line.

using a resolution of 1920 × 1080 pixels, and images were calibrated using an object of known size in the focal plane. Typical resolutions were around 17 pixels per mm.

Trigonometric relations were used to calculate the radius of the liquid-air interface from the width. Figure 4(c) shows the cross-section of a liquid column between a cylinder of radius b and a flat plate. The angle α spanned by the wetted perimeter of the cylinder cross-section is related to the corresponding wetted length a of the plate by the equation

$$\frac{a}{b} = \sin\alpha + (1 - \cos\alpha)\tan\frac{\alpha}{2}. \tag{7.4}$$

The radius of the interface is related to the separation and the wetted angle by

$$\frac{s}{b} = \frac{1 - \cos\alpha}{\cos\theta + \cos(\theta + \alpha)}. \tag{7.5}$$

When $\theta = 0$, we recover the result given by Princen (1969) for a cylinder in contact with a plate.

7.2. *Results and discussion*

In this section, results of the experiments are reported and discussed. Videos were analyzed to obtain two types of data: (1) the location $z^*(t)$ of the tip of the liquid column as a function of time, and (2) profiles of the interface radius $s(z, t)$ as a function of the axial coordinate for selected times.

The location of the tip as a function of time is shown in figure 5 for two different oils and two different cylinder radii. The altitude of the tip is plotted as a function of the time on linear axes in figure 5(a). Figure 5(b) shows the same data scaled using (5.1a,b,c) and plotted on logarithmic axes along with the solution (5.12) using the dimensionless tip altitude $\eta^* = 1.5761$, which corresponds to $n = 2$. In figure 5(a), we observe that the trajectories for a single fluid (silicone oil) in corners created by cylinders of two different radii are nearly coincident prior to scaling, which supports the hypothesis that the cylinder radius does not affect the evolution of the tip altitude. Since (5.1a,b,c) does not involve the gap geometry, this overlap persists in figure 5(b) after the tip altitude and time have been non-dimensionalized. Although the oils have different viscosities, capillary lengths, and contact angles, the trajectories all collapse onto the same curve after scaling.

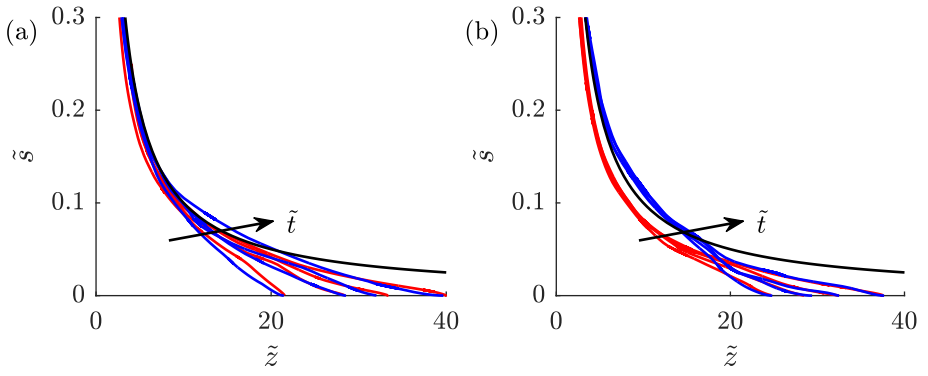

FIGURE 6. Interface radius as a function of altitude rescaled using (5.1a,b,c). Data are shown for $b = 9$ mm in red and $b = 4$ mm in blue. The equilibrium profile (5.3) is shown in black. (a) Data acquired for silicone oil ($\theta = 0$) at $\tilde{t} = 4450, 8900, 13350, 22250$ for both radii. (b)Data acquired for mineral oil ($\theta = 20°$) at $\tilde{t} = 6750, 10120, 13490, 20240$.

The comparison in figure 5(b) shows that it requires a time of $10^2 - 10^3 \mu \ell_{cg}/\gamma$ in order to approach the similarity solution, which is natural owing to the time required to evolve into a slender flow configuration and to enter the regime in which the intermediate asymptotics are relevant. Other possible contributors to the initial transients are discussed by Quéré (1997) and Clanet & Quéré (2002). At long times, the tip progresses as approximately $\tilde{t}^{1/3}$, which agrees with experimental and numerical results due to Higuera *et al.* (2008) for linear corners, and with experimental observations of Ponomarenko *et al.* (2011) for power-law corners with linear, quadratic, and cubic ($n = 3$) corners.

We further investigate the validity of the model by examining the interface radius as a function of the altitude at different times. Figure 6 shows profiles of the interface radius at different times acquired for cylinder radii $b = 4$ mm and $b = 9$ mm using silicone oil (figure 6(a)) and mineral oil (figure 6(b)). The data is shown rescaled according to (5.1a,b,c). For the data acquired using both oils, we observe that the tip altitudes for both radii at each of the times are nearly coincident, which is to be expected given the agreement in figure 5. In figure 6(a), the profiles acquired using silicone oil for the two radii also nearly overlap. This agreement between rescaled data for cylinder radii that differ by more than a factor of two suggests that the corner geometry affects neither the interface radius nor the tip altitude and supports the use of the characteristic scales in (5.1a,b,c), which do not depend on the geometric constant c.

However, there are discrepancies between the profiles for different radii for the data acquired using mineral oil in figure 6(b). Although there is good agreement between the profiles for the different radii near the tip, the two sets of profiles diverge as they approach the reservoir. The improved agreement towards the tip of the column may be attributed to greater accuracy at higher altitudes of the approximations associated with the assumption of a long and narrow column geometry. Specifically, the assumption is made that the incline of the triple line is negligible and thus the angle between the free surface and the solid surface is the contact angle θ, and this assumption leads to the relation (2.3). When the contact angle is zero, which is the case for the data shown in figure 6(a) obtained using silicone oil, the angle in the cross-section and the contact angle are the same, but the difference between them would become more significant as the contact angle increases, e.g. when mineral oil, which has a contact angle of 20°, is used.

Then, we proceed to test the validity of the similarity solution using the experimental

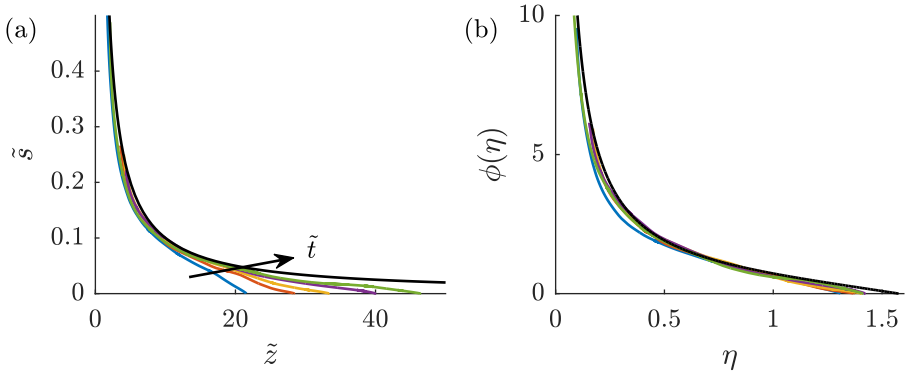

FIGURE 7. Interface radius as a function of altitude at dimensionless times $\tilde{t} = 4450, 8900, 13350, 22250, 35600$ for silicone oil with $b = 9$ mm. (a) Non-dimensionalized profiles. The equilibrium profile (5.3) is shown in black. (b) Profiles transformed using (5.6). The solution to the ODE (5.7) with $n = 2$ is shown in black.

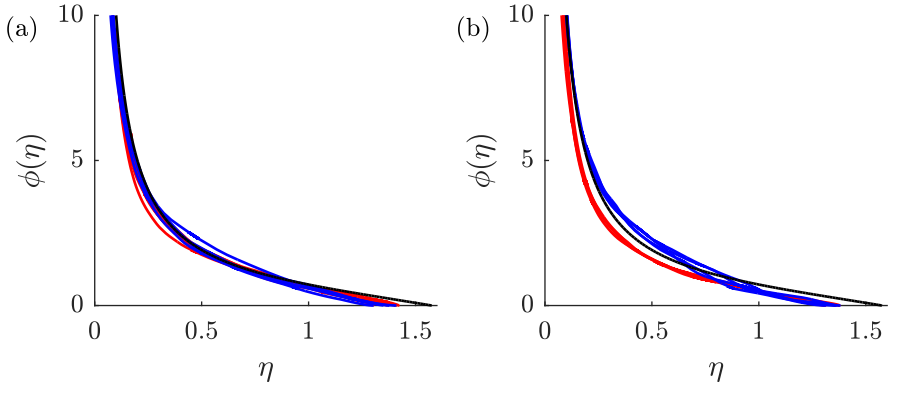

FIGURE 8. Interface radius as a function of altitude from experiments using different oils and cylinder radii. Data are shown for $b = 9$ mm in red and $b = 4$ mm in blue. The profiles have been transformed using the similarity transformation (5.6). The solution to the ODE (5.7) shown in black. (a) Data acquired for silicone oil ($\theta = 0^\circ$) at $\tilde{t} = 4450, 8900, 13350, 22250$ for both radii and additionally $\tilde{t} = 35600$ for $b = 9$ mm. (b) Data acquired for mineral oil ($\theta = 20^\circ$) at $\tilde{t} = 6750, 10120, 13490, 20240$.

data. Figure 7 shows the profiles of the interface radius at five different times for silicone oil rising in a corner created using a cylinder of radius $b = 9$ mm. In figure 7(a), the profiles after scaling with (5.1a,b,c) and prior to applying the similarity transformation (5.6) are shown. As in figure 6, we observe that the tip altitude advances with time and that the profile extends to greater altitudes while gradually converging to the equilibrium curve (5.3). After applying the transformation in (5.6), the curves at the different times collapse onto the solution of (5.7).

In the results presented and discussed thus far, it is apparent that experimental data departs from the theoretical predictions near the advancing front. In figure 5(b), we observe that the scaled tracks of the tip altitude lie slightly below the prediction (5.12) obtained by scaling and solving the differential equation. This behavior was also observed by Higuera *et al.* (2008), who found that the ODE solution overestimated the measured front location. The overestimation of the front location is related to the discrepancy between the predicted and measured self-similar profiles in figure 7. Specifically, while the measured profiles appear to collapse well with the similarity transformation, the

self-similar curve departs from the theoretical curve near the tip of the column, such that the location of the tip in the measurements ultimately falls short of the predictions. Considering the simplifying assumptions used in the development of the model, there are several possible reasons for why this may be the case. For example, it was assumed that the contact angle always takes its equilibrium value, which may not be true for an advancing liquid front. Furthermore, we have neglected van der Waals forces, which become important at the small length scales found near the tip of the column. Investigations by Gurumurthy *et al.* (2018) of the formation of tongues or rivulets of liquids due to capillary rise in the sharp corners in closed polygonal capillaries show that the size of the capillary influences the prefactor for the power law. Effects on the equilibrium meniscus shape and the boundary condition near the reservoir (e.g., due to confinement by solid walls in polygonal channels) may alter the dynamics and shape of the rising column.

In figure 8, profiles of the interface radius, transformed according to the similarity solution (5.6), from experiments conducted using silicone oil in corners created by two cylinder radii $b = 4$ mm and $b = 9$ mm, are shown. In figure 8(a), we observe that for experiments conducted using silicone oil, profiles of the interface radius for the two cylinder radii, when transformed, collapse onto the same curve. However, as discussed previously, the agreement is not perfect for the mineral oil experiments represented in figure 8(b), which is likely due to the non-zero contact angle. The profiles for each cylinder radius appear to be self-similar, but these self-similar profiles are distinct from each other and from the theoretical curve except for the region close to the tip of the column.

8. Conclusion

We have investigated capillary rise of a liquid into a sharp corner formed by the contact of two power-law surfaces $h_i(x) = c_i x^n$, $i = 1, 2$ for $n \geqslant 1$. Lubrication theory was used to derive the PDE describing the evolution of the liquid column in the corner and investigated the effects of corner geometry on various aspects of the phenomenon, specifically rate of capillary rise and the geometry of the liquid column which is formed. It is found that flow rate and area depend on the combined parameter $c = c_2 - c_1$, and that when the evolution equation is expressed in terms of the interface radius s, the parameter c is absent so that the corner geometry enters only through the power n. Consequently, the characteristic scales for time, the altitude of the column tip, and the interface radius are independent of the corner geometry, i.e., they are universal. In addition, we identified a geometry-independent similarity transformation, confirming the universality of the $t^{1/3}$ power-law of capillary rise. The prefactor η^* in the power-law is the dimensionless tip altitude, which depends only on n and monotonically decreases from $\eta^* \approx 1.6718$ at $n = 1$ to $\eta^* \approx 1.4378$ as $n \to \infty$. Due to the universality of the scaling and the similarity transformation, the profiles of the interface radius for a given power n are the same regardless of the value of c. These results are experimentally verified using oils with different equilibrium contact angles, among other fluid properties. Measurements of capillary rise generally agreed well with the theory, but some disagreement is observed for the experimentally obtained profiles for a nonzero contact angle, indicating that the contact angle affects the limits of validity of the model.

Acknowledgements

This material is based upon work supported by the National Science Foundation Graduate Research Fellowship under Grant No. DGE-2039656. The research was supported partially by NSF via grant CBET-2127563 (to HAS).

The authors thank anonymous reviewers for their comments and suggestions for improving the manuscript. We are grateful to Udi Yariv for helpful discussions.

Declaration of Interests

The authors report no conflict of interest.

Appendix A

In this appendix, we formulate the capillary rise problem in terms of the width of the liquid column for ease of comparison with prior treatments of this problem by Higuera *et al.* (2008) and Zhou & Doi (2020). By substituting for the interface radius $s(z,t)$ using a rearrangement of (2.3),

$$s = \frac{c}{2\cos\theta} w^n, \tag{A 1}$$

the PDE (4.6) may be expressed as

$$\frac{\partial}{\partial t}\left(w^{n+1}\right) = \frac{\gamma\cos^2\theta}{3\mu}\frac{n+1}{3n+1}\frac{\partial}{\partial z}\left\{w^{n+1}\left[\left(\frac{c}{2\cos\theta}\right)\frac{\partial}{\partial z}(w^n) + \left(\frac{c}{2\cos\theta}\right)^2\frac{w^{2n}}{\ell_{cg}^2}\right]\right\}. \tag{A 2}$$

The PDE (A 2) corresponds exactly to equation (3.6) in (Zhou & Doi 2020). The finite volume condition (3.10) is

$$\int_0^\infty w^{n+1}(z,t)\mathrm{d}z < \infty \qquad \text{for} \qquad 0 \leqslant t < \infty, \tag{A 3}$$

and the boundary condition (4.2) becomes

$$\rho g z = \frac{2\gamma\cos\theta}{c w^n} \qquad \text{as} \qquad z \to 0. \tag{A 4}$$

Then, scaling the variables by

$$\tilde{z} = \frac{z}{\ell_{cg}(\cos\theta)^{1/2}}, \qquad \tilde{w} = \frac{w}{\left[2c^{-1}\ell_{cg}(\cos\theta)^{1/2}\right]^{1/n}}, \qquad \text{and} \qquad \tilde{t} = \frac{\gamma(\cos\theta)^{1/2}t}{3\mu\ell_{cg}} \tag{A 5a,b,c}$$

allows us to write (A 2), (A 3), and (A 4) in dimensionless form

$$\frac{\partial}{\partial\tilde{t}}\left(\tilde{w}^{n+1}\right) = \frac{n+1}{3n+1}\frac{\partial}{\partial\tilde{z}}\left\{\tilde{w}^{n+1}\left[\frac{\partial}{\partial\tilde{z}}(\tilde{w}^n) + \tilde{w}^{2n}\right]\right\}, \tag{A 6}$$

$$\int_0^\infty \tilde{w}^{n+1}(z,t)\mathrm{d}z < \infty \qquad \text{for} \qquad 0 \leqslant t < \infty, \tag{A 7}$$

and

$$\tilde{z} = \frac{1}{\tilde{w}^n} \qquad \text{as} \qquad \tilde{z} \to 0. \tag{A 8}$$

The PDE (A 6) admits a similarity transformation of the form

$$\tilde{w}(z,t) = \tilde{t}^{-1/3n}\psi(\eta) \qquad \text{where} \qquad \eta = \tilde{t}^{-1/3}\tilde{z}, \tag{A 9}$$

by which we obtain the ODE

$$-\frac{1}{3}\eta\frac{\mathrm{d}}{\mathrm{d}\eta}\left(\psi^{n+1}\right)=\frac{n+1}{3n+1}\frac{\mathrm{d}}{\mathrm{d}\eta}\left[\psi^{n+1}\left(\frac{\mathrm{d}}{\mathrm{d}\eta}\left(\psi^{n}\right)+\psi^{2n}\right)\right] \tag{A 10}$$

and the conditions

$$\int_0^\infty \psi^{n+1}(z,t)\mathrm{d}z<\infty \qquad \text{for} \qquad 0\leqslant t<\infty, \tag{A 11}$$

and

$$\eta=\frac{1}{\psi^n} \qquad \text{as} \qquad \eta\to 0. \tag{A 12}$$

As discussed in Appendix B, the finite volume condition implies that ψ becomes zero at some finite η^*,

$$\psi(\eta)=0 \qquad \eta\geqslant\eta^*. \tag{A 13}$$

The boundary condition at the tip is

$$[\psi^n(\eta)]'=-\frac{3n+1}{3(n+1)}\eta^*, \tag{A 14}$$

and the solution near the tip behaves as

$$\psi(\eta)=\left[\frac{3n+1}{3(n+1)}\eta^*(\eta^*-\eta)\right]^{1/n} \tag{A 15}$$

which may be compared with (3.23) in Zhou & Doi (2020).

Appendix B

In this appendix, several consequences of the finite volume constraint (5.8*b*) are shown following similar reasoning as that used by Romero & Yost (1996) in their analysis of flow into a horizontal groove. First, it is shown that the extent of the liquid column is finite. Then, a boundary condition at the liquid front is derived. For convenience we reproduce the ODE (5.7), boundary condition (5.8*a*), and volume constraint inequality (5.8*b*) here:

$$-\frac{1}{3}\eta\left[\phi^{1+1/n}(\eta)\right]'=\frac{n+1}{3n+1}\left[\phi^{1+1/n}(\eta)\left(\phi'(\eta)+\phi^2(\eta)\right)\right]', \tag{B 1a}$$

$$\phi(\eta)=\frac{1}{\eta} \quad \text{as} \quad \eta\to 0 \qquad \text{and} \tag{B 1b}$$

$$\int_0^\infty \phi^{1+1/n}(\eta)\mathrm{d}\eta<\infty, \tag{B 1c}$$

where primes indicate differentiation with respect to the argument of the function. We begin by noting that for a non-negative monotonically decreasing function $\phi(\eta)$, (B 1*c*) implies

$$\lim_{\eta\to\infty}\phi(\eta)=0, \tag{B 2a}$$

$$\lim_{\eta\to\infty}\eta\phi^{1+1/n}(\eta)=0, \qquad \text{and} \tag{B 2b}$$

$$\lim_{\eta\to\infty}\phi'(\eta) \quad \text{finite}. \tag{B 2c}$$

A function $\phi(\eta)$ may satisfy (B 2a) either by asymptotically approaching zero as η approaches infinity, in which case the function is nonzero (and positive) for all η; or by reaching zero at a finite value η^* and remaining zero, in which case the function is nonzero for the finite range $0 \leqslant \eta < \eta^*$, or in other words the function has finite support. It will be shown that functions ϕ satisfying (B 1a) cannot asymptotically approach zero and instead must become zero at some finite η^*, which is the location of the tip of the liquid column. Then, a boundary condition at that location will be derived.

Making use of the equality $[\eta\phi^{1+1/n}(\eta)]' = \phi^{1+1/n}(\eta) + \eta[\phi^{1+1/n}(\eta)]'$, we rewrite the left side of (B 1a) as

$$-\frac{1}{3}\left[[\xi\phi^{1+1/n}(\xi)]' - \phi^{1+1/n}(\xi)\right] = \frac{n+1}{3n+1}\left[\phi^{1+1/n}(\xi)\left[\phi'(\xi)+\phi^2(\xi)\right]\right]', \tag{B 3}$$

where we have introduced the dummy variable ξ. We rearrange terms,

$$\left[\frac{n+1}{3n+1}\phi^{1+1/n}(\xi)\left[\phi'(\xi)+\phi^2(\xi)\right] + \frac{1}{3}\xi\phi^{1+1/n}(\xi)\right]' = \frac{1}{3}\phi^{1+1/n}(\xi), \tag{B 4}$$

then integrate (B 4) from η to $\tilde{\eta}$,

$$\frac{n+1}{3n+1}\phi^{1+1/n}(\xi)\left(\phi'(\xi)+\phi^2(\xi)\right) + \frac{1}{3}\xi\phi^{1+1/n}(\xi)\Big|_{\eta}^{\tilde{\eta}} = \frac{1}{3}\int_{\eta}^{\tilde{\eta}}\phi^{1+1/n}(\xi)\mathrm{d}\xi, \tag{B 5}$$

which leads to

$$\begin{aligned}\frac{n+1}{3n+1}\phi^{1+1/n}(\tilde{\eta})\left(\phi'(\tilde{\eta})+\phi^2(\tilde{\eta})\right) + \frac{1}{3}\tilde{\eta}\phi^{1+1/n}(\tilde{\eta}) \\ - \frac{n+1}{3n+1}\phi^{1+1/n}(\eta)\left(\phi'(\eta)-\phi^2(\eta)\right) - \frac{1}{3}\eta\phi^{1+1/n}(\eta) = \frac{1}{3}\int_{\eta}^{\tilde{\eta}}\phi^{1+1/n}(\xi)\mathrm{d}\xi.\end{aligned} \tag{B 6}$$

Taking the limit of (B 6) as $\tilde{\eta}\to\infty$ and applying (B 2a), (B 2b), and (B 2c), we eliminate the first two terms on the left side,

$$-\phi^{1+1/n}(\eta)\left[\frac{n+1}{3n+1}\left[\phi'(\eta)+\phi^2(\eta)\right] + \frac{1}{3}\eta\right] = \frac{1}{3}\int_{\eta}^{\infty}\phi^{1+1/n}(\xi)\mathrm{d}\xi. \tag{B 7}$$

Then due to (B 1c)

$$\phi^{1+1/n}(\eta)\left[\frac{n+1}{3n+1}\left[\phi'(\eta)+\phi^2(\eta)\right] + \frac{1}{3}\eta\right] \leqslant 0 \qquad \forall\eta. \tag{B 8}$$

If $\phi(\eta)$ approached zero asymptotically as $\eta\to\infty$, then we would require

$$\frac{n+1}{3n+1}\left[\phi'(\eta)+\phi^2(\eta)\right] + \frac{1}{3}\eta \leqslant 0 \qquad \forall\eta. \tag{B 9}$$

However, since $\phi^2(\eta)\to 0$ as $\eta\to\infty$ (a consequence of (B 2a)), (B 9) implies that $\phi'(\eta)\to-\infty$ as $\eta\to\infty$, which contradicts (B 2c). Therefore, we conclude that $\phi(\eta)$ must become zero at some finite η^* and remain zero as η increases; that is,

$$\phi(\eta) = 0 \qquad \eta \geqslant \eta^*. \tag{B 10}$$

Now, we derive a boundary condition at η^*. Due to (B 10), we may let $\tilde{\eta} = \eta^*$ in (B 6) instead of taking the limit $\eta\to\infty$,

$$-\phi^{1+1/n}(\eta)\left\{\frac{n+1}{3n+1}\left[\phi'(\eta)+\phi^2(\eta)\right] + \frac{1}{3}\eta\right\} = \frac{1}{3}\int_{\eta}^{\eta^*}\phi^{1+1/n}(\xi)\mathrm{d}\xi. \tag{B 11}$$

We proceed by defining a function $f(\eta)$ such that

$$\frac{1}{3}\int_{\eta}^{\eta^*} \phi^{1+1/n}(\xi)\mathrm{d}\xi = \phi^{1+1/n}(\eta)f(\eta), \tag{B 12}$$

which is non-negative and monotonically decreasing. By applying L'Hôpital's rule to evaluate the limit of $f(\eta)$ as η approaches η^*, it can also be shown that $f(\eta)$ has the property

$$\lim_{\eta\to\eta^*} f(\eta) = 0. \tag{B 13}$$

Substituting (B 12) into (B 11) and dividing by $\phi^{1+1/n}(\eta)$, we are left with

$$-\frac{n+1}{3n+1}\left[\phi'(\eta) + \phi^2(\eta)\right] - \frac{1}{3}\eta = f(\eta). \tag{B 14}$$

Then, taking the limit of (B 14) as $\eta \to \eta^*$ and applying (B 10) and (B 13), we obtain the boundary condition

$$\phi'(\eta^*) = -\frac{3n+1}{3(n+1)}\eta^*. \tag{B 15}$$

Finally, we observe that this derivation is essentially equivalent to the method used by Higuera *et al.* (2008) and Zhou & Doi (2020) to identify the boundary condition at the tip of the liquid column. In the limit $\eta \to \eta^*$, that is, when $\eta^* - \eta$ is small, the column geometry is described by

$$\phi'(\eta) = -\frac{3n+1}{3(n+1)}\eta^*. \tag{B 16}$$

Integrating and applying the boundary condition $\phi(\eta^*) = 0$ yields the approximate solution near $\eta = \eta^*$,

$$\phi(\eta) = \frac{3n+1}{3(n+1)}\eta^*(\eta^* - \eta), \tag{B 17}$$

which has the same structure as the boundary conditions presented by Higuera *et al.* (2008) and Zhou & Doi (2020) (see appendix A for further details).

Appendix C

The ODE for the self-similar profile of the liquid column (5.7) can be arranged as follows to obtain a form more suited for numerical simulations:

$$\phi''(\eta) = -\phi^{-1}(\eta)\phi'(\eta)\left[\frac{3n+1}{n}\left(\frac{1}{3}\eta + \phi^2\right) + \frac{n+1}{n}\phi'(\eta)\right]. \tag{C 1}$$

The shooting method was applied using the two conditions

$$\phi(\eta^*) = 0 \qquad \text{and} \tag{C 2}$$

$$\phi'(\eta^*) = -\frac{3n+1}{3(n+1)}\eta^* \tag{C 3}$$

to find the value of η^* (to the fourth decimal place) for which the solution converged to the equilibrium solution

$$\phi(\eta) = \frac{1}{\eta} \tag{C 4}$$

as $\eta \to 0$. The results are tabulated in table 3.

n	η^*	$(3n+1)/3(n+1)$
1	1.6718	0.6667
2	1.5761	0.7778
3	1.5355	0.8883
4	1.5124	0.8667
5	1.4978	0.8889
10	1.4672	0.9394
20	1.4508	0.9683
30	1.4449	0.9785
50	1.4405	0.9869
100	1.4362	0.9934
200	1.4350	0.9967
500	1.4334	0.9987
3000	1.4329	0.9998
10000	1.4326	0.9999
20000	1.4326	1.0000

TABLE 3. Dimensionless tip altitudes η^* and the magnitude of the numerical prefactor for different n.

In order to avoid the singularity when $\phi(\eta) = 0$, the ODE was solved using the initial condition

$$\phi(\eta^*) = 1 \times 10^{-11} \tag{C 5}$$

instead of (C 2). Solutions were obtained using the NDSolve function in Mathematica, Version 13.1 (Wolfram Research, Inc.).

REFERENCES

AYYASWAMY, P. S., , I. CATTON & EDWARDS, D. K. 1974 Capillary flow in triangular grooves. *J. Appl. Mech.* .

BARENBLATT, G. I. 2003 *Scaling*. Cambridge University Press.

BATCHELOR, G. K. 1967 *An Introduction to Fluid Dynamics*. Cambridge University Press.

BELL, J. M. & CAMERON, F. K. 1906 The flow of liquids through capillary spaces. *The Journal of Physical Chemistry* **10** (8), 658–674.

BERTHIER, E., DOSTIE, A.M., LEE, U.N., BERTHIER, J. & THEBERGE, A.B. 2019 Open microfluidic capillary systems. *Analytical Chemistry* **91** (14), 8739–8750.

BLUMAN, G.W. & KUMEI, S. 2013 *Symmetries and Differential Equations*. Springer Science & Business Media.

BOUSSINESQ, J. 1868 Mémoire sur l'influence des frottements dans les mouvements réguliers des fluids. *Journal de Mathématiques Pures et Appliquées* **13** (2), 377–424.

CAI, J., CHEN, Y., LIU, Y., LI, S. & SUN, C. 2022 Capillary imbibition and flow of wetting liquid in irregular capillaries: A 100-year review. *Advances in Colloid and Interface Science* **304**, 102654.

CLANET, C. & QUÉRÉ, D. 2002 Onset of menisci. *Journal of Fluid Mechanics* **460**, 131–149.

Concus, Paul & Finn, Robert 1969 On the behavior of a capillary surface in a wedge. *Proceedings of the National Academy of Sciences* **63** (2), 292–299.

Debnath, L. 2005 *Nonlinear partial differential equations for scientists and engineers*. Springer.

Di, Y., Xu, X. & Doi, M. 2016 Theoretical analysis for meniscus rise of a liquid contained between a flexible film and a solid wall. *Europhysics Letters* **113** (3), 36001.

Duprat, C 2022 Moisture in textiles. *Annual Review of Fluid Mechanics* **54**, 443–467.

Duprat, C., Aristoff, J. M. & Stone, H. A. 2011 Dynamics of elastocapillary rise. *Journal of Fluid Mechanics* **679**, 641–654.

Eggers, J. & Fontelos, M. A. 2015 *Singularities: Formation, Structure, and Propagation*. Cambridge University Press.

de Gennes, P.-G., Brochard-Wyart, F. & Quéré, D. 2004 *Capillarity and Wetting Phenomena: Drops, Bubbles, Pearls, Waves*. Springer.

Gurumurthy, V. T., Rettenmaier, D., Roisman, I. V., Tropea, C. & Garoff, S. 2018 Computations of spontaneous rise of a rivulet in a corner of a vertical square capillary. *Colloids and Surfaces A: Physicochemical and Engineering Aspects* **544**, 118–126.

Hauksbee, F. 1706 VIII. An experiment made at Gresham-College, shewing that the seemingly spontaneous ascention of water in small tubes open at both ends is the same in vacuo as in the open air. *Philosophical Transactions of the Royal Society of London* **25** (305), 2223–2224.

Hauksbee, F. 1712 X. An account of an experiment touching the ascent of water between two glass planes, in an hyperbolick figure. *Philosophical Transactions of the Royal Society of London* **27** (336), 539–540.

Higuera, F. J., Medina, A. & Linan, A. 2008 Capillary rise of a liquid between two vertical plates making a small angle. *Physics of Fluids* **20** (10), 102102.

Hooke, R. 1661 An attempt for the explanation of the phenomena observable in an experiment published by the Honourable Robert Boyle. *Printed by JH for Sam. Thomson, London* .

Jurin, J. 1717 II. An account of some experiments shown before the Royal Society; with an enquiry into the cause of the ascent and suspension of water in capillary tubes. *Philosophical Transactions of the Royal Society of London* **30** (355), 739–747.

Laplace, P.-S. 1806 Traité de mécanique céleste; suppléments au Livre X, 1805 and 1806 resp. *Œuvres Complete* **4**.

Lenormand, R. & Zarcone, C. 1984 Role of roughness and edges during imbibition in square capillaries. In *SPE Annual Technical Conference and Exhibition*. OnePetro.

Lucas, R. 1918 Ueber das zeitgesetz des kapillaren aufstiegs von flüssigkeiten. *Kolloid-Zeitschrift* **23** (1), 15–22.

Ponomarenko, A., Quéré, D. & Clanet, C. 2011 A universal law for capillary rise in corners. *Journal of Fluid Mechanics* **666**, 146–154.

Princen, H. M. 1969 Capillary phenomena in assemblies of parallel cylinders: I. Capillary rise between two cylinders. *Journal of Colloid and Interface Science* **30** (1), 69–75.

Quéré, D. 1997 Inertial capillarity. *Europhysics Letters* **39** (5), 533.

Ransohoff, T. C. & Radke, C. J. 1988 Laminar flow of a wetting liquid along the corners of a predominantly gas-occupied noncircular pore. *Journal of Colloid and Interface Science* **121** (2), 392–401.

Reyssat, M., Courbin, L., Reyssat, E. & Stone, H. A. 2008 Imbibition in geometries with axial variations. *Journal of Fluid Mechanics* **615**, 335–344.

Romero, L. A. & Yost, F. G. 1996 Flow in an open channel capillary. *Journal of Fluid Mechanics* **322**, 109–129.

Stone, H. A. 2005 On lubrication flows in geometries with zero local curvature. *Chemical Engineering Science* **60** (17), 4838–4845.

Tang, L.-H. & Tang, Y. 1994 Capillary rise in tubes with sharp grooves. *Journal de Physique II* **4** (5), 881–890.

Taylor, B. 1710 IX. Part of a letter from Mr. Brook Taylor, F.R.S. to Dr. Hans Sloane R.S. Secr. concerning the ascent of water between two glass planes. *Philosophical Transactions of the Royal Society of London* **27** (336), 538–538.

Warren, Patrick B 2004 Late stage kinetics for various wicking and spreading problems. *Physical Review E* **69** (4), 041601.

Washburn, E. W. 1921 The dynamics of capillary flow. *Physical Review* **17** (3), 273.

Weislogel, M. M. & Lichter, S. 1998 Capillary flow in an interior corner. *Journal of Fluid Mechanics* **373**, 349–378.

Zhou, J. & Doi, M. 2020 Universality of capillary rising in corners. *Journal of Fluid Mechanics* **900**, A29.